# Illuminating the structure of convective cold pools with a dense station network

Bastian Kirsch[1,4], Cathy Hohenegger[2,4], Daniel Klocke[3,4,2], Rainer Senke[1], Michael Offermann[1], and Felix Ament[1,2,4]

[1]Meteorological Institute, University of Hamburg, Germany
[2]Max Planck Institute for Meteorology, Hamburg, Germany
[3]Deutscher Wetterdienst, Offenbach am Main, Germany
[4]Hans Ertel Centre for Weather Research, Branch Model Development - Convection, Hamburg, Germany

**Correspondence:** Bastian Kirsch (bastian.kirsch@uni-hamburg.de)

**Abstract.** From June to August 2020 an observational network of 103 meteorological ground-based stations covered the greater area ($50\,\mathrm{km}\times35\,\mathrm{km}$) of Hamburg (Germany) as part of the Field Experiment on Sub-mesoscale Spatio-Temporal variability in Hamburg (FESST@HH). The purpose of the experiment was to shed light on the sub-mesocale ($\mathcal{O}(100)\,\mathrm{m} - \mathcal{O}(10)\,\mathrm{km}$) structure of convective cold pools that typically remains under-resolved in operational networks. During the experiment, 82 custom-built, low-cost APOLLO (Autonomous cold POoL LOgger) stations sampled air temperature and pressure with fast-response sensors at $1\,\mathrm{s}$ resolution to adequately capture the strong and rapid perturbations associated with propagating cold pool fronts. A secondary network of 21 weather stations with commercial sensors provided additional information on relative humidity, wind speed and precipitation at $10\,\mathrm{s}$ resolution. The realization of the experiment during the COVID-19 pandemic was facilitated by a large number of volunteers who provided measurement sites on their premises and supported the station maintenance. This article introduces the novel type of autonomously operating instruments, their measurement characteristics and the FESST@HH data set (https://doi.org/10.25592/UHHFDM.8973; Kirsch et al., 2021b). A case study demonstrates that the network is capable of mapping the horizontal structure of the temperature signal inside a cold pool as well as quantifying its size and propagation velocity throughout its life cycle. Beyond its primary purpose, the data set offers new insights into the spatial and temporal characteristics of the nocturnal urban heat island and variations of turbulent temperature fluctuations as an expression of different urban and natural environments.

## 1 Introduction

We present the instrumentation and data set of the Field Experiment on Sub-mesoscale Spatio-Temporal variability in Hamburg (FESST@HH) that illuminates the spatial and temporal structure of convective cold pools. Conventional meteorological station networks have a typical resolution of $\sim25\,\mathrm{km}$ in space and $10\,\mathrm{min}$ in time and are essential to obtain a reliable picture of the atmospheric background state. Remote sensing techniques help us to retrieve more-finely resolved information for a few atmospheric variables like precipitation or wind speed. However, the spatial variability of basic meteorological parameters like air temperature or pressure on the sub-mesoscale (i.e., length scales between $\mathcal{O}(100)\,\mathrm{m}$ and $\mathcal{O}(10)\,\mathrm{km}$) remains under-resolved.

The information on sub-mesoscale variability is especially important for the investigation and simulation of convective clouds and precipitation (Stevens et al., 2020). Convective cold pools are an important source of this variability and, therefore, represent a blind spot for conventional observation networks. This fact qualifies them as the main motivation for the FESST@HH experiment.

Cold pools play a prominent role for understanding the formation and life cycle of atmospheric convection. They are defined as areas of relatively cool and dense air that form through melting and evaporation of hydrometeors underneath precipitating clouds. Their horizontal size range from a few km to several tens of km (Terai and Wood, 2013; Feng et al., 2015) with temperature falling by more than 10 K (Engerer et al., 2008; Kirsch et al., 2021a). As the body of cold air grows and propagates away from the precipitation, it often causes a rapid decrease in local air temperature and the formation of a gust front. Secondary updrafts are preferentially triggered in the region ahead of the cold pool air due to the combination of mechanical lifting and accumulation of moisture in the lower troposphere (Tompkins, 2001; Feng et al., 2015; Torri et al., 2015). Cold pools are also found to support the organization of convective clouds and the transition from shallow to deep convection (Khairoutdinov and Randall, 2006; Schlemmer and Hohenegger, 2014; Kurowski et al., 2018). Since models with hectometer-scale resolution are required to realistically represent processes related to convection (Bryan et al., 2003; Grant and Heever, 2016; Hirt et al., 2020), large-eddy simulations (LES) have become an established tool to study cold pools. However, LES models critically depend on parametrizations of subgrid-scale phenomena, such as turbulence and microphysics (Daw; Li et al., 2015). This fact supports the need for observational data with a similar resolution to LES models that facilitate validation of simulations and enhance our understanding of sub-mesoscale processes.

Observational studies on cold pools draw upon a wide range of data-collection methods. These include measurements from boundary layer towers (Goff, 1976; Kirsch et al., 2021a), aircrafts (Terai and Wood, 2013), ships (Szoeke et al., 2017), precipitation radars (Borque et al., 2020), and combinations thereof (Mueller and Carbone, 1987; Feng et al., 2015). Nevertheless, capturing the horizontal structure of cold pools with the help of in situ observations is a challenging task given the small number of studies using, e. g., mesoscale station networks (Markowski et al., 2002; Engerer et al., 2008). In a recent study, van den Heever et al. (2021) described the use of uncrewed aerial systems, radiosondes and surface stations during the C³LOUD-Ex campaign to characterize the structure of convective updrafts and downdrafts on scales between $\mathcal{O}(100)\,\mathrm{m}$ and $\mathcal{O}(1)\,\mathrm{km}$, whereas their surface network consisted of only three points. There are also examples of more extensive observation networks at km-scale resolution, like the the Oklahoma City Micronet (Basara et al., 2011) and the WegenerNet (Kirchengast et al., 2014). However, with respect to areal coverage and instrument characteristics, these networks were mainly designed for climate monitoring rather than investigating short-lived convective-scale processes like cold pools.

The FESST@HH field experiment took place in Hamburg (Germany) from June to August 2020. The idea of the experiment was to perform meteorological observations that are suited to capturing the spatial structure of cold pools at the sub-mesoscale. This goal required the design of a ground-based station network that is large enough to cover the typical size of a cold pool ($\mathcal{O}(10)\,\mathrm{km}$) and dense enough to satisfy the desired resolution ($\mathcal{O}(100)\,\mathrm{m}$). Additionally, the measurement instruments had to be equipped with appropriate sensors for capturing cold pool fronts but still cheap enough to be deployed in large numbers. The relatively long measurement period was chosen to catch a reasonable number of cold pools during the convective season

in Hamburg, where around seven events per month are expected (Kirsch et al., 2021a). In this article, we introduce the novel instruments and data set of FESST@HH and demonstrate its potential for investigating the spatial structure and life cycle of cold pools based on a case study. Moreover, the experimental setup allows to study the spatial dimension of the nocturnal urban heat island as well as the variability of turbulent temperature fluctuations in different environments. A special feature of FESST@HH was the participation of a large number of volunteers that became necessary in response to the COVID-19 pandemic.

## 2  Design of instruments

The instrument design for the FESST@HH experiment was guided by the technical demands required to observe the submesoscale structure of cold pools in space and time. Most importantly, the instruments had to be equipped with fast-response air temperature sensors that precisely capture relative changes in temperature. The sampling interval required was $\Delta t \leq 10\,\mathrm{s}$ in order to track the propagation of cold pool fronts with a velocity of about $10\,\mathrm{m\,s^{-1}}$ (Borque et al., 2020) on scales of $\mathcal{O}(100)\,\mathrm{m}$. Moreover, the instruments had to operate independent of an external power source for about two weeks to facilitate the search for appropriate site locations. According to these requirements, we designed and manufactured the Autonomous cold POoL LOgger (APOLLO) for operation during the FESST@HH experiment. We complemented the network with WXT weather stations based on commercial sensors.

### 2.1  APOLLO

The APOLLO is a simple and low-cost data logger that records air temperature and pressure. Inspired by the pyranometer network stations used during the HOPE campaign (Madhavan et al., 2016), it operates autonomously without an external power source and its sensor and control units are mounted on a short mast (Fig. 1). The APOLLO is equipped with a fast-response and moisture-resistant thermometer consisting of a small ($7\,\mathrm{mm} \times 1.2\,\mathrm{mm}$) NTC (negative temperature coefficient) thermistor probe (type: TE Connectivity GA10K3MRBD1; Fig. 2a) placed inside a radiation shield (see sensor specifications in Table 1). The design and size of the sensor allow for very small response times according to a time constant $\tau = 14\,\mathrm{s} \pm 10\,\%$ at $3\,\mathrm{m\,s^{-1}}$ wind speed that we determined in wind tunnel laboratory tests. The control unit is based on a micro controller board (type: HIMALAYA Matrix-Core ESP32) located inside a small ($26\,\mathrm{cm} \times 17\,\mathrm{cm} \times 10\,\mathrm{cm}$) logger box (Fig. 2b). A digital air pressure sensor (type: Bosch BME280 Environmental sensor) is installed on the logger main board, whereas a counterbalance valve ensures rapid adjustment of barometric pressure inside the logger box.

The readings of the temperature and pressure sensors are sampled with a resolution of $1\,\mathrm{s}$ and written onto a micro-SD memory card. An on-board GPS receiver is used to initially synchronize the internal real-time clock on start of the logger. To minimize power consumption during operation, the GPS module is activated to log the current time only once per hour for about $10\,\mathrm{s}$, which allows to correct the logger time stamp for drifting in a post-processing step. The logger can establish a local WiFi hotspot for on-site control and data inspection and is able to send status telegrams via the LoRa (Long Range) wireless communication protocol for live monitoring.

The APOLLO is powered by a standard USB power bank battery (20 Ah capacity) that corresponds to an autonomous operation time of 10 to 14 days. For easy access during maintenance, the power bank is placed inside a separate plastic tube. All logger units are mounted on a 3 m mast that is anchored in the soil with a ground screw. In the standard configuration, the temperature sensor at the top of the mast and the pressure sensor inside the logger box are situated about 2.9 m and 1.7 m above ground, respectively. The material costs for all required parts sum up to around 300 Euro per logger.

The APOLLO station proves suitable for accurately recording cold pool front passages in field measurements. The comparison with an inertia-free ultrasonic sensor confirms that the NTC thermometer responds almost instantaneously to the rapid cooling signature of a cold pool event and even captures high-frequency temperature fluctuations (Fig. 3). Test measurements also show that external site conditions, such as surrounding obstacles or different surface properties, do not have a considerable impact on the cold pool signal (not shown) and, therefore, do not restrict the choice of the measurement site.

## 2.2 WXT weather station

WXT weather stations are employed to complement the APOLLO stations by providing information on other common meteorological parameters at selected locations. The main component of the station is a commercial compact multi-parameter sensor (type: Vaisala Weather Transmitter WXT536) that measures air pressure, temperature, relative humidity, wind speed, wind direction and precipitation (see sensor specifications in Table 2). Pressure, temperature and relative humidity measurements are performed by a PTU module inside a radiation shield that combines a capacitive silicon BAROCAP sensor (pressure), a resistive thin-film Pt1000 sensor (temperature) and a capacitive thin-film polymer HUMICAP R2 sensor (relative humidity). Wind speed and wind direction are detected by an WINDCAP ultrasonic anemometer on top of the radiation shield that consists of three equally-spaced ultrasonic transducers on a horizontal plane. The wind measurements are determined from the transit times of the ultrasound along the three paths with a sampling rate of 4 Hz and are internally averaged. The precipitation measurement principle of the WXT536 sensor is based on a RAINCAP piezoelectrical sensor underneath a steel cover that detects the impacts of individual rain drops within a collecting area of 60 cm$^2$. Since the individual signals are proportional to the size of the rains drops, the sensor is able to derive the accumulated rainfall amount within the measurement interval. The sensor also distinguishes between impacts of rain drops and hail stones (Vaisala, 2020). Additionally, the WXT station is equipped with an external Pt1000 thermometer (type: TMH cable sensor Pt1000 1/3 DIN Klasse B; size: 40 mm×3 mm) inside a separate radiation shield that allows for smaller response times of the measured temperature signal ($\tau =$55 s±10 % at 3 m s$^{-1}$ wind speed) than the internal PTU module ($\tau =$213 s±10 % at 3 m s$^{-1}$ wind speed).

The WXT data are sampled at 10 s resolution and written onto a SD memory card by a data logger (type: Avisaro M22766) that is synchronized with an integrated GPS module. The units of the station are powered by a 12 V lead battery. The battery is recharged by a solar panel (67 cm×41 cm) so that the station can operate autonomously for several months, depending on the available sun light. Similar to the APOLLO design, the station components are mounted on a 3 m mast that is anchored in the soil with a ground screw (Fig. 4).

## 3 Description of experiment

The FESST@HH measurement campaign took place under extraordinary circumstances. Its name is a modification of the acronym FESSTVaL (Field Experiment on Sub-mesoscale Spatio-Temporal Variability in Lindenberg), a field campaign that

125 was originally planned to take place at the Meteorological Observatory Lindenberg (eastern Germany) during summer 2020. Due to travel restrictions in response to the COVID-19 pandemic, the decision was made to postpone the FESSTVaL campaign to 2021 and to replicate the cold pool part of FESSTVaL in Hamburg under the name FESST@HH to make it compatible with home-office regulations.

### 3.1 Experiment area

130 Hamburg is the second largest city in Germany (population: 1.9 million; 2019) and is located in northern Germany (53.5° N, 10.0° E) about 80 km from the North Sea and the Baltic Sea. The FESST@HH measurement sites cover an area of 50 km×35 km that includes the urban center of Hamburg and its rural surroundings (Fig. 5). The station network consists of 82 APOLLO sites (Table 3) and 21 WXT sites (Table 4) that are randomly scattered over the domain with the tendency for a higher station density closer to the city center. The random arrangement results from the location of private gardens and of public facilities

135 like schoolyards that could be used as measurement sites (see section 3.2). The average nearest-neighbor distance between all 103 measurement sites is 1.85±1.42 km, whereas it is 1.93±1.41 km and 5.49±1.98 km for APOLLO and WXT, respectively. The measurement area is crossed by the Elbe river in southeast–northwest direction and is characterized by relatively flat terrain. While the Elbe valley is situated around sea level, the elevation north and south of it does not exceed about 80 m and 110 m, respectively. The altitude of all measurement site lies between 1 m and 82 m above sea level with an average of 17 m.

140 To characterize the environmental properties of the measurement sites, we apply the local climate zone (LCZ) framework introduced by Stewart and Oke (2012). This framework classifies the impact of surface structure, surface cover and human activity on the local thermal climate with the help of 17 standardized LCZ classes. All 103 FESST@HH sites fall into 15 different LCZ classes, which also includes combinations of classes to describe the heterogeneity within about 500 m around the station (Bechtel et al., 2015). The majority of sites (61) are situated in an open arrangement of low-rise buildings and

145 scattered trees (LCZ 6; *mixed* in Fig. 5), while 24 sites, mostly near the city center, are located in the proximity of mid-rise and high-rise buildings, either in a compact or open arrangement (LCZ 2, 4 and 5; *urban*). Each of the other occurring classes contain less than ten sites, which include natural environments (LCZ 9, A, B and D) and industrial areas with mostly paved surfaces (LCZ 8 and 10). 10 sites are situated near large water bodies like the Elbe river, the Alster lake, or channels (LCZ G).

### 3.2 Implementation

150 The installation of instruments started in late May 2020 and took about 3 weeks. The measurement period covered all three summer months and ended in early September 2020. The realization of the experiment was enabled by the support of many institutions and private landowners who provided permissions at short notice for using their premises as measurement sites. The different groups of landowners are indicated by two-letter acronyms as part of a unique site identifier code that also

contains the site number and the installed instrument type (a=APOLLO, w=WXT). The majority of measurement stations
155  were installed in private gardens and backyards (PG; Fig. 6a) as well as on the grounds of various institutions and clubs
(OG). Further groups of sites include existing weather stations and sites of the Meteorological Institute (WS and MI), air
quality observation sites of the Free and Hanseatic City of Hamburg (LM), grounds of the University of Hamburg (UH), and
schoolyards (KB). A special characteristic of the latter group is that most of the respective APOLLO logger components are
mounted at existing weather stations used for educational purposes and, therefore, exhibit lower temperature sensor heights
160  ($\sim$1.8 m) than the standard stations (Fig. 6b). Further deviations from the standard APOLLO installation include four loggers
mounted on balconies (040UHa, 092PGa, 111OGa, and 113PGa; Fig. 6e) and two WXT stations installed on top of a container
(017LMw; Fig. 6g) and on a roof-deck of the building of the Meteorological Institute (114UHw; Fig. 6h). Due to technical
issues, minor changes to the instrumental set up had to be implemented during the measurement period with the replacement
of one APOLLO (068OGa) and two WXT stations (048OGw and 114UHw) as well as the replacement of one APOLLO by a
165  WXT station (083PGa).

Ensuring the implementation of FESST@HH was compatible with home-office not only affected the selection of measurement sites but also the maintenance strategy. Instead of a small team servicing the entire network, the maintenance work was
shared between nearly 40 people. Private landowners, who provided measurement sites in their backyard, could also volunteer
to regularly change the battery, check the data and upload it to a FTP server. Other stations located on public ground, school-
170  yards or industrial premises were serviced by colleagues living nearby. The main benefit of this maintenance strategy was that
the collective effort kept the individual workload very low and promoted the continuous operation of the instruments, which
eventually eased the execution of the experiment under challenging circumstances.

## 4 Data processing

The processing of the APOLLO and WXT station measurement data is a two-stage procedure. This study describes the pub-
175  lished level 2 data format that contains quality-controlled data in a standardized format. In contrast, level 0 data are the raw data
as directly produced by the instruments and level 1 data are homogenized data for preliminary analyses, but have not passed
any quality checks.

### 4.1 Level 0 data

The raw measurement data are stored in ASCII files. The APOLLO data logger creates a new file at the start time, which
180  contains the internal logger time, the GPS-synchronized time, the resistance readings of the NTC thermometer, the pressure
readings of the BME280 module and status information at 1 Hz frequency. In contrast, new level 0 WXT data files are created
at midnight on a daily basis. Each line in the files consists of a GPS-synchronized time stamp and the measurement telegram
of a specific sensor module, whereas each module sends data at 10 s intervals.

## 4.2 Level 1 data

185 Measurement data, which have passed the first processing step, are called level 1 data. At this stage, basic standardization procedures are performed to allow for easy access to the data for preliminary analyses, but not quality checks. Most importantly, this includes the correction and homogenization of the data time stamps. For the APOLLO data, the internal logger time is corrected with its deviation from the most recent valid GPS time stamp that is logged once per hour. Data for missing time steps are filled with placeholder values (NaN). Furthermore, daily files are created by splitting multi-day files and merging 190 sub-daily files. In case of the WXT data, all time stamps are moved to a regular 10 s time grid. The measurement data itself are not manipulated, except for the APOLLO thermometer readings that are converted from resistance to temperature. For both station types, level 1 data are stored in a standard ASCII format.

## 4.3 Level 2 data

The purpose of the second processing level is to generate a standardized and quality-controlled data product that is ready to 195 use for scientific analyses. Since the raw APOLLO measurements contain different kinds of erroneous data, which originate from technical issues of the logger or characteristics of the measurement site, we apply several quality checks and corrections to clean up the data. This processing step is not required for WXT data due to internal quality checks implemented by the manufacturer of the sensor. In total, less than $1\%$ of the level 1 data fail the quality criteria and need to be removed. The correction procedure contains the following steps:

200     – removing erroneous temperature and pressure data outside plausible limits defined by $0 \leq T \leq 40\,°C$ and $950 \leq p \leq 1050\,hPa$, respectively;

    – removing spikes in temperature (pressure) larger than $\Delta T = 0.5\,K$ ($\Delta p = 1\,hPa$), where $\Delta T$ ($\Delta p$) denotes the absolute difference from the 30 s (60 s) running median value. For the temperature data, spikes are only removed for phases of active WiFi connection, which produces the spikes;

205     – removing temperature data showing implausibly large differences from the current network mean value defined as $|T - \overline{T}| > 15\,K$. For three stations with erroneous NTC temperature sensor (037UHa, 040UHa, 068OGa), a criterion of $|T - \overline{T}| > 2\,K$ is applied and all data within a time window of 15 min before and after erroneous data are also removed;

    – manually removing single periods of erroneous temperature and pressure measurements that are not filtered by the previous criteria. In case of station 039UHa, temperature measurements on more than 40 days are affected by the warm 210      air outlet of a near by air conditioning facility and are manually removed;

    – applying a 10 s running mean smoothing procedure on the temperature measurements of station 113PGa to account for an anomalously high noise level of the NTC sensor;

    – correcting the individual biases of NTC temperature sensors. The biases are determined from a one week long calibration with respect to a reference WXT sensor (114UHw);

215    Level 2 data are stored in the NetCDF4 data format (Eaton et al., 2017), while the naming of files, variables and attributes complies with the SAMD (Standardized Atmospheric Measurement Data) Product Standard (Lammert et al., 2018). Accordingly, all measurement data of the same variable and from the same type of instrument are merged and stored in daily files. The file header contains all relevant meta data describing the individual measurement sites, namely the station identifier, the station name, the geographic coordinates, the altitude above sea level, the sensor height above ground and the LCZ.

## 5    Description of data set

### 5.1    Data availability

The level 2 data set of FESST@HH covers the period from 1 June to 31 August 2020 (Fig. 7a). The average availability of valid temperature observations is 83.2 % and 87.6 % for all APOLLO and WXT stations, respectively. Since the 3 month period also includes the installation phase of the instruments during the first half of June, these numbers increase to 90.0 % and 94.3 % if only the period after 15 June is considered. During this period, the daily availability of APOLLO and WXT measurements is always larger than 82.6 % and 90.0 %, respectively. Apart from the removed measurements affected by erroneous sensors and local site conditions, most of the data gaps in the APOLLO data are due to missing power supply of the loggers, either caused by technical issues related to the power bank batteries or insufficient maintenance. In only one case was a battery stolen. The higher stability of the power supply is also the reason for the generally higher availability of WXT data compared to APOLLO data.

### 5.2    Weather conditions

The weather conditions during the FESST@HH period covered the full range of a typical mid-latitude summer. The air temperature measured by the station network ranges between a minimum of $5.3\,^\circ$C on 13 July and a maximum of $35.6\,^\circ$C on 8 August (Fig. 7b). During the entire 92 day period, the maximum temperature exceeded $25\,^\circ$C on 41 days and $30\,^\circ$C on 16 days, including an exceptionally long period of 12 consecutive days with more than $30\,^\circ$C between 6 August and 17 August. In contrast, July was characterized by a phase of relatively cold temperatures with a maximum of above $25\,^\circ$C on only 6 days. Rainfall, defined as a daily rainfall accumulation of more than $1\,$mm at at least one WXT station of the network, was observed on half of the days from 1 June to 31 August (Fig. 7c). On 11 days, mostly between 27 June and 10 July, the median rainfall amount exceeded $5\,$mm. A maximum daily accumulation of $28.2\,$mm was observed on 27 June when a strong convective event occurred.

## 6    Observations of sub-mesoscale phenomena

The goal of the FESST@HH experiment was to design and operate an observation network that is dense enough to investigate the structure of convective cold pools. However, the data set also contains information and potential scientific implications for further sub-mesoscale phenomena that we present here.

## 6.1 Cold pools

During the 3 month measurement period, 37 cold pool events occurred, defined by at least five stations satisfying the cold pool detection criterion introduced by Kirsch et al. (2021a), i. e., a local temperature drop of at least 2 K within 30 min associated with rainfall. To demonstrate the ability of the station network to capture the characteristics of a cold pool and to shed light on its internal structure, we present one case study.

On 10 August 2020 around 12:45 UTC, a strong and nearly stationary convective precipitation cell developed southeast of the city center. About 10 min later, the formation of a cold pool became evident from a rapid cooling of the surface-layer air masses. Fig. 8 illustrates the evolution of the cold pool with snapshots of the temperature perturbations relative to the pre-event state observed by the station network. About 20 min after initiation of the convective cell, the cold pool exhibited a temperature perturbation of up to -8 K within an area of less than 10 km in diameter (Fig. 8a). After another 20 min, the cold pool deepened to about -11 K and expanded to a size of roughly 10 km×20 km (Fig. 8b). This process continued until around 14:00 UTC when the cold pool reached its maximum temperature perturbation of about -12 K and a diameter of nearly 30 km, whereas the northeastern parts of the cold pool were outside of the network (Fig. 8d). The associated near-surface wind field observed by the WXT weather stations indicated a strong divergent flow at the cold pool center, especially during the early stages of its life cycle (Fig. 8a and b). Consistent with expected characteristics of a cold pool, the radial expansion of the cold air masses during the later stages was also present in the wind observations, predominantly southwest of the cold pool center (Fig. 8c and d).

The time series of temperature measurements at selected stations of the network provide further insights into the spatial structure and life cycle of the cold pool (Fig. 9a). APOLLO station *Luxweg* (104PGa) near the cold pool origin experienced an initial temperature drop of approximately 8 K within 5 min that continued at a slower rate afterwards and reached its maximum perturbation of -12 K after one hour. This value is on the order of strongest temperature perturbations expected during cold pool passages in Hamburg (Kirsch et al., 2021a). The readings of the stations *Ochsenwerder Norderdeich* (082PGa) and *Obsthof Lehmbeck* (054OGa), located 4 km and 12 km further south, respectively, reveal that the maximum cooling decreases to about one-third away from the center, which suggests a highly heterogeneous temperature structure inside the cold pool. Since the site *Luftmessnetz Habichtstraße* (018LMa), situated northwest of the cold pool center, experienced no cooling at all, the cold pool produced a temperature gradient of 12 K within a distance of 11 km. This result is in line with the findings of van den Heever et al. (2021) who report a variation of near-surface cold pool properties on scales between $\mathcal{O}(100)$ m and $\mathcal{O}(1)$ km. The time lags between the cooling signals observed on the southern side of the cold pool also allow us to estimate its propagation velocity. Based on time lags of about 15 min and 50 min for travel distances of 3.9 km (104PGa–082PGa) and 11.9 km (104PGa–054PGa), respectively, the velocity is of about 4 m s$^{-1}$. This value lies in the expected range (Borque et al., 2020), considering that the parent precipitation cell was almost stationary and, therefore, did not superimpose the buoyancy-driven propagation of the cold air.

The accompanying air pressure measurements at the four selected sites confirm that the negative temperature perturbation of the cold pool is associated with a typical hydrostatic pressure rise (Fig. 9b). However, the positive pressure perturbation was well-pronounced only at station 104PGa, while the amplitudes were not proportional to the strength of the corresponding

cooling signals. The pressure signal at station 104PGa also experienced rapid fluctuations of about 1 hPa that were not apparent
at the three other sites. Although an in-depth investigation of such effects lies beyond the scope of this study, this may indicate
that the spatial structure of a cold pool differs between temperature and pressure and that mechanisms other than the hydrostatic
cooling control the pressure signal near the center.

## 6.2  Urban heat island

The FESST@HH data set is well suited for studying urban climate effects as the station network covers both the city center
and its rural surrounding. Stations near the city center record weather conditions with urban modifications, whereas rural
stations provide undisturbed references. Focusing on air temperature, we define the urban modification $\Delta T_{\mathrm{city}}$ as the difference
between the locally observed air temperature and the undisturbed, natural temperature $T_{\mathrm{nat}}$, determined exclusively by large-
scale weather conditions. On scales of $\mathcal{O}(10)\,\mathrm{km}$ without orography, it is reasonable to assume that $T_{\mathrm{nat}}$ varies only linearly
in space. We estimate the mean and the slope of this linear temperature field with a regression using all stations in weakly
sealed environments, i.e., all stations with a maximum sealing up to *open low-rise* (LCZ 6). The mean diurnal cycle of $\Delta T_{\mathrm{city}}$
features a step function at almost all stations (Fig. 10a). During daytime, the urban effects are small and $\Delta T_{\mathrm{city}}$ is close to zero
everywhere. In contrast, during nighttime, predominantly between 21 and 3 UTC, $\Delta T_{\mathrm{city}}$ reaches a constant level at all stations,
which largely reflects the well-known nocturnal urban heat island effect. For example, the most central station *Wetterstation
HafenCity* (010WSa; orange in Fig. 10a) is almost 2.5 K warmer than estimated $T_{\mathrm{nat}}$ and the most rural site *Obsthof Schuback*
(055OGw) is even 1.5 K colder than the reference. The spatial pattern of the mean nocturnal urban heat excess is in agreement
with the typical heat island structure featuring largest values close to the city center (Fig. 10b). Further analysis of individual
days (not shown) provides indication that the advection of the heat island effect causes downwind heat plumes to form, which
affect specific outskirts depending on the prevailing wind direction.

## 6.3  Turbulent temperature fluctuations

The NTC temperature sensor of the APOLLO station responds rapidly to air temperatures fluctuations. The recorded time
series with a sampling rate of 1 Hz partly resolves temperature eddies related to turbulent sensible heat fluxes. The high
frequency temperature fluctuation expressed by the standard deviation of temperature readings within 1 min intervals, $\sigma_{\mathrm{T}}$,
features a well-pronounced diurnal cycle (Fig. 11a). During nighttime, $\sigma_{\mathrm{T}}$ is close to 0.05 K at all stations, which most likely
resembles the noise level of the instruments. However, at daytime, $\sigma_{\mathrm{T}}$ is well above that noise level and follows the common
diurnal cycle of net radiation or sensible heat flux at the surface. Turbulent fluxes are strongly determined by the local surface
condition like albedo, sealing or vegetation cover. Likewise, the differences in the diurnal cycle of $\sigma_{\mathrm{T}}$ can be explained by
local surface conditions: the station *Stadtteilschule Blankenese* (033KBa) at a schoolyard next to a sportsground (low albedo,
no evapotranspiration) with free insolation exhibits the highest temperature variability. High values also occur at the schoolyard
of station *Schule Redder* (036KBa) but are shifted and limited to morning hours due to a building west of the station casting
a shadow and reflecting sunlight. Even more extreme, buildings shade the station *Luftmessnetz Rothenburgsort* (020LMa)
almost the whole day except during the late afternoon. The lowest temperature variance is observed at station *Uni Sternwarte*

(043UHa), the only station below tall trees. The heat exchange within the tree canopy effectively reduced the energy exchange at the ground.

The relation between surface heat exchange and temperature variability is also directly confirmed by correlating the net radiation observed at the Hamburg weather mast reference site (Bruemmer et al., 2012) with $\sigma_T$ at the neighboring APOLLO station *Wetterstation Zollamt* (011WSa) located about 750 m away (Fig. 11b). Values of $\sigma_T$ lower than 0.75 K are strongly correlated to situations where the net radiation is close to zero. Increasing variance beyond this threshold is mostly explained by increasing net radiation ($r^2$=0.77). Instead of the sensible heat flux, we use the net radiation for this analysis to minimize the influence of land surface differences between the two sites (pasture at *Wetterstation Zollamt* versus sealed area at Hamburg weather mast). Additional measurements on a test site show that the heating of the sensor shield by solar radiation does not impact $\sigma_T$ (not shown). This finding supports our reasoning that the APOLLO stations capture turbulent temperature fluctuations that are mainly caused by the surface heat exchange in the near environment of the observation site.

## 7    Summary and conclusions

The FESST@HH field experiment took place in Hamburg (Germany) from June to August 2020 with the primary aim of illuminating the internal structure of convective cold pools that conventional observations miss. To this end, a dense network of 103 autonomously operating weather stations was installed over an area of 50 km×35 km with an average distance between the stations of 1.85km. The measurements were mainly conducted by 82 low-cost, custom-built APOLLO stations that were designed to sample the strong and rapid changes in air temperature and pressure associated with cold pools at 1 s resolution. Additional measurements of relative humidity, wind speed and precipitation at 10 s resolution were performed by 21 WXT weather stations based on commercial sensors.

The FESST@HH data set is unique not only with respect to its scientific potential for investigating sub-mesoscale atmospheric processes but also with respect to its implementation. The experiment was successfully conducted despite the exceptional circumstances caused by the COVID-19 pandemic, especially thanks to the short-notice support of local institutions and private landowners, who provided their ground as measurement sites and helped with the station maintenance. The low-cost and self-manufactured measurement instruments operated smoothly without any major technical problems, although they were never used in such a large number before. The good performance is reflected by an availability of quality-controlled data of more than 90 % during the main observation period. Most importantly, a case study demonstrates that the network is capable of mapping the sharp horizontal temperature gradients produced by a convective cold pool and capturing its spatial footprint. Throughout its life cycle, the cold pool diameter grows from less than 10 km to nearly 30 km, while its leading edge propagates at a velocity of about 4 m s$^{-1}$ away from the center of convection. There is also evidence that the spatial variance of the corresponding pressure signals differs from the cooling signature and may indicate the presence of non-hydrostatic effects acting within the cold pool center. Furthermore, the data set is relevant for studies in urban meteorology as the dense temperature observations include information on the spatial structure of the nocturnal urban heat island as well as on the local surface heat exchange mirrored by high-frequency temperature fluctuations.

345 The FESST@HH field experiment proves that it is possible to conduct observations that close the information gap left by conventional measurement networks. In addition, it highlights the real need for dense station networks that act like a magnifying glass for sub-mesoscale atmospheric processes. The use of a large number of low-cost instruments designed for a specific purpose has shown to be a feasible strategy to tailor a measurement network that is dense enough to shed light on previously unobserved scales. These data are scientifically valuable not only for a deeper understanding of cold pools and the

350 convective life cycle, but also for the validation of hectometer-scale numerical simulations. Moreover, the data set leaves space for unexpected results and applications not yet anticipated. FESST@HH also exemplifies how a major community effort can ease the execution of a major scientific enterprise or – as in this case – make it possible at all. In this sense, FESST@HH has the potential to be a prototype for future field campaigns. It already provides a prove of concept for an extended investigation of cold pools and further sub-mesoscale boundary layer structures during the FESSTVaL 2021 experiment.

355 ## 8  Data availability

The data set is available at https://doi.org/10.25592/UHHFDM.8973 (Kirsch et al., 2021b). The file size per day and measurement variable is about 25 MB and 1.5 MB for APOLLO and WXT data, respectively.

*Author contributions.*  BK wrote the manuscript (except for sections 6.2 and 6.3), processed the data, performed the cold pool analyses, helped to design, assemble and test the instruments and to install and service the measurement stations. CH and DK conceptualized the

360 idea for the experiment. RS designed, assembled and tested the APOLLO hardware and software. MO designed the components and technical infrastructure of the APOLLO and WXT stations and helped to service them. FA prepared sections 6.2 and 6.3 and performed the corresponding analyses, helped to design the instruments, plan the experiment and service the stations.

*Competing interests.*  The authors declare that they have no conflict of interests.

*Acknowledgements.*  We are grateful to Marco Clemens and Ingo Lange for heavily supporting the manufacturing, installation and mainte-

365 nance of measurement stations and to Sarah Wiesner for planning and coordinating the field experiment. We thank Theresa Szyszka and Jan Moritz Witt for assembling the APOLLO logger main boards, manufacturing the components of the APOLLO and WXT stations and supporting their maintenance. For either helping with the installation and maintenance of stations or providing ground for measurement sites we are thankful to Sigrid and Werner Bock, Agnes Bornholdt, Frank Böttcher, Burghardt Brümmer, Stefan Bühler, Finn Burgemeister, Guido Cioni, Martin Claussen, Traute Crüger, Henning Dorff, Tobias Finn, Veronika Gayler, David Grawe, Akio Hansen, Anja Hermans,

370 Tatiana Ilyina, Olaf Jäke, Markus Kilian, Stefan Kinne, Marlene and Reinhard Kirsch, Brita Kliemt, Hartmut Kock, Heike Konow, Sascha Krueck, Heiner Meier, Ulrike Niemeier and Luis Kornblueh, Peter Peitzner, Jon Petersen, Thomas Raddatz, Jule Radtke, Berinike Rappat, Florian Römer, Nicole and Steffen Rüeß, Rita Schierholz, Imke Schirmacher, Hauke Schmidt, Amelie Schmitt, Hauke Schulz, Constanze

Seibert, Milica Stankovic, Claudia Timmreck and Hannes Thiemann, Karla Tomhawe, Bodo Voigt, Stefan Walter, Ralf Wedemann, Tobias Weiß, Susanne and Heinz-Dieter Wenck, Benjamin Will, Holger Witt, and Florian Ziemen. We also acknowledge the following institu-
375 tions, schools, clubs and companies for allowing us to install measurement stations on their grounds: Hamburger Luftmessnetz, Universität Hamburg, Bundesanstalt für Wasserbau Hamburg, Deutscher Wetterdienst Niederlassung Hamburg, Drachenfreunde Winsen, Greenpeace Wilhelmsburg, Gut Karlshöhe, Gymnasium Rahlstedt, Halepaghen-Schule Buxtehude, Hamburger Aero-Club Boberg, Hamburger Bogen-schützen Gilde, Hansa Sportverein Stöckte, Hochschule für Angewandte Wissenschaften Hamburg, Immanuel-Kant-Gymnasium Harburg, Obsthof Axel Schuback, Obsthof Lehmbeck, Overmeyer Landbaukultur, Restaurant Bobby Reich, Restaurant Fährhaus Tatenberg, Schule
380 Redder Sasel, Segelclub Rhe Hamburg, Segelvereinigung Sinstorf, Stadtteilschule Blankenese, Stadtteilschule Eidelstedt, Stadtteilschule Meiendorf, Suntrace, Tennisclub Eichtalpark, and TSV Holm.

This research was carried out in the Hans Ertel Center for Weather Research (HErZ). This German research network of universities, research institutions, and the German Weather Service (DWD) is funded by the BMVI (Federal Ministry of Transport and Digital Infrastructure).

385 BK is thankful to Jochem Marotzke and Dallas Murphy for providing valuable tips on the writing style and structure of the manuscript and to Arjun Kumar for proofreading.

# References

Comparison of evaporation and cold pool development between single-moment and multimoment bulk microphysics schemes in idealized simulations of tornadic thunderstorms, Mon. Weather Rev., 138, https://doi.org/10.1175/2009MWR2956.1.

Basara, J. B., Illston, B. G., Fiebrich, C. A., Browder, P. D., Morgan, C. R., McCombs, A., Bostic, J. P., McPherson, R. A., Schroeder, A. J., and Crawford, K. C.: The Oklahoma City Micronet, Meteorol. Appl., 18, 252–261, https://doi.org/10.1002/MET.189, 2011.

Bechtel, B., Alexander, P. J., Böhner, J., Ching, J., Conrad, O., Feddema, J., Mills, G., See, L., and Stewart, I.: Mapping local climate zones for a worldwide database of the form and function of cities, ISPRS Int. J. Geo-Inf., 4, 199–219, https://doi.org/10.3390/ijgi4010199, 2015.

Borque, P., Nesbitt, S. W., Trapp, R. J., Lasher-Trapp, S., and Oue, M.: Observational study of the thermodynamics and morphological characteristics of a midlatitude continental cold pool event, Mon. Weather Rev., 148, 719–737, https://doi.org/10.1175/MWR-D-19-0068.1, 2020.

Bosch: BME280 data sheet, version 1.9, https://www.bosch-sensortec.com/media/boschsensortec/downloads/datasheets/bst-bme280-ds002.pdf, accessed on 14 January 2021, 2020.

Bruemmer, B., Lange, I., and Konow, H.: Atmospheric boundary layer measurements at the 280 m high Hamburg weather mast 1995–2011: Mean annual and diurnal cycles, Meteorol. Z., 21, 319–335, https://doi.org/10.1127/0941-2948/2012/0338, 2012.

Bryan, G. H., Wyngaard, J. C., and Fritsch, J. M.: Resolution requirements for the simulation of deep moist convection, Mon. Weather Rev., 131, 2394–2416, https://doi.org/10.1175/1520-0493(2003)131<2394:RRFTSO>2.0.CO;2, 2003.

Crameri, F.: Scientific colour maps, version 7.0.1, https://doi.org/10.5281/zenodo.1243862, 2018.

Crameri, F., Shephard, G. E., and Heron, P. J.: The misuse of colour in science communication, Nat. Commun., 11, 5444, https://doi.org/10.1038/s41467-020-19160-7, 2020.

Eaton, B., Gregory, J., Drach, B., Taylor, K., Hankin, S., Blower, J., Caron, J., Signell, R., Bentley, P., Rappa, G., Höck, H., Pamment, A., Juckes, M., and Raspaud, M.: NetCDF Climate and Forecast (CF) Metadata Conventions version 1.7, p. 156, https://cfconventions.org/Data/cf-conventions/cf-conventions-1.7/cf-conventions.pdf, accessed on 14 January 2021, 2017.

Engerer, N. A., Stensrud, D. J., and Coniglio, M. C.: Surface characteristics of observed cold pools, Mon. Weather Rev., 136, 4839–4849, https://doi.org/10.1175/2008MWR2528.1, 2008.

Feng, Z., Hagos, S., Rowe, A. K., Burleyson, C. D., Martini, M. N., and Szoke, S. P. D.: Mechanisms of convective cloud organization by cold pools over tropical warm ocean during the AMIE/DYNAMO field campaign, J. Adv. Model Earth Sy., 7, 357–381, https://doi.org/10.1002/2014MS000384, 2015.

Goff, R. C.: Vertical structure of thunderstorm outflows, Mon. Weather Rev., 104, 1429–1440, https://doi.org/10.1175/1520-0493(1976)104<1429:VSOTO>2.0.CO;2, 1976.

Grant, L. D. and Heever, S. C. v. d.: Cold pool dissipation, J. Geohphys. Res.-Atmos., 121, 1138–1155, https://doi.org/10.1002/2015JD023813, 2016.

Hirt, M., Craig, G. C., Schäfer, S. A. K., Savre, J., and Heinze, R.: Cold-pool-driven convective initiation: using causal graph analysis to determine what convection-permitting models are missing, Q. J. Roy. Meteor. Soc., 146, 2205–2227, https://doi.org/10.1002/QJ.3788, 2020.

Khairoutdinov, M. and Randall, D.: High-resolution simulation of shallow-to-deep convection transition over land, J. Atmos. Sci., 63, 3421–3436, https://doi.org/10.1175/JAS3810.1, 2006.

Kirchengast, G., Kabas, T., Leuprecht, A., Bichler, C., and Truhetz, H.: WegenerNet: A pioneering high-resolution network for monitoring weather and climate, Bull. Am. Meteorol. Soc., 95, 227–242, https://doi.org/10.1175/BAMS-D-11-00161.1, 2014.

425 Kirsch, B., Ament, F., and Hohenegger, C.: Convective cold pools in long-term boundary layer mast observations, Mon. Weather Rev., 149, 811–820, https://doi.org/10.1175/MWR-D-20-0197.1, 2021a.

Kirsch, B., Hohenegger, C., Klocke, D., Senke, R., Offermann, M., and Ament, F.: FESST@HH meteorological network measurements, version v00, https://doi.org/10.25592/UHHFDM.8973, 2021b.

Kurowski, M. J., Suselj, K., Grabowski, W. W., and Teixeira, J.: Shallow-to-deep transition of continental moist convection: Cold pools, 430 surface fluxes, and mesoscale organization, J. Atmos. Sci., 75, 4071–4090, https://doi.org/10.1175/JAS-D-18-0031.1, 2018.

Lammert, A., Grützun, V., and Stamnas, E.: The SAMD product standard (Standardized Atmospheric Measurement Data), https://doi.org/10.5281/ZENODO.1741364, 2018.

Li, Z., Zuidema, P., Zhu, P., and Morrison, H.: The sensitivity of simulated shallow cumulus convection and cold pools to microphysics, J. Atmos. Sci., 72, 3340–3355, https://doi.org/10.1175/JAS-D-14-0099.1, 2015.

435 Madhavan, B. L., Kalisch, J., and Macke, A.: Shortwave surface radiation network for observing small-scale cloud inhomogeneity fields, Atmos. Meas. Tech., 9, 1153–1166, https://doi.org/10.5194/AMT-9-1153-2016, 2016.

Markowski, P. M., Straka, J. M., and Rasmussen, E. N.: Direct surface thermodynamic observations within the rear-flank downdrafts of nontornadic and tornadic supercells, Mon. Weather Rev., 130, 1692–1721, https://doi.org/10.1175/1520-0493(2002)130<1692:DSTOWT>2.0.CO;2, 2002.

440 Mueller, C. K. and Carbone, R. E.: Dynamics of a thunderstorm outflow, J. Atmos. Sci., 44, 1879–1898, https://doi.org/10.1175/1520-0469(1987)044<1879:DOATO>2.0.CO;2, 1987.

Schlemmer, L. and Hohenegger, C.: The formation of wider and deeper clouds as a result of cold-pool dynamics, J. Atmos. Sci., 71, 2842–2858, https://doi.org/10.1175/JAS-D-13-0170.1, 2014.

Stevens, B., Acquistapace, C., Hansen, A., Heinze, R., Klinger, C., Klocke, D., Rybka, H., Schubotz, W., Windmiller, J., Adamidis, P., Arka, 445 I., Barlakas, V., Biercamp, J., Brueck, M., Brune, S., Buehler, S. A., Burkhardt, U., Cioni, G., Costa-Suros, M., Crewell, S., Crueger, T., Deneke, H., Friederichs, P., Henken, C. C., Hohenegger, C., Jacob, M., Jakub, F., Kalthoff, N., Koehler, M., van Laar, T. W., Li, P., Loehnert, U., Macke, A., Madenach, N., Mayer, B., Nam, C., Naumann, A. K., Peters, K., Poll, S., Quaas, J., Roeber, N., Rochetin, N., Scheck, L., Schemann, V., Schnitt, S., Seifert, A., Senf, F., Shapkalijevski, M., Simmer, C., Singh, S., Sourdeval, O., Spickermann, D., Strandgren, J., Tessiot, O., Vercauteren, N., Vial, J., Voigt, A., and Zaengl, G.: The Added Value of Large-eddy and Storm-resolving 450 Models for Simulating Clouds and Precipitation, J. Meteorol. Soc. Jpn., 98, 395–435, https://doi.org/10.2151/JMSJ.2020-021, 2020.

Stewart, I. D. and Oke, T. R.: Local climate zones for urban temperature studies, Bull. Am. Meteorol. Soc., 93, 1879–1900, https://doi.org/10.1175/BAMS-D-11-00019.1, 2012.

Szoeke, S. P. D., Skyllingstad, E. D., Zuidema, P., and Chandra, A. S.: Cold pools and their influence on the tropical marine boundary layer, J. Atmos. Sci., 74, 1149–1168, https://doi.org/10.1175/JAS-D-16-0264.1, 2017.

455 TE Connectivity: High humidity environments mini probe (MRBD), https://www.te.com/commerce/DocumentDelivery/DDEController? Action=showdoc&DocId=Data+Sheet%7FMRBD_10K3MRBD1%7FA%7Fpdf%7FEnglish%7FENG_DS_MRBD_10K3MRBD1_A. pdf%7FGA10K3MRBD1, accessed on 7 October 2021, 2015.

Terai, C. R. and Wood, R.: Aircraft observations of cold pools under marine stratocumulus, Atmos. Chem. Phys., 13, 9899–9914, https://doi.org/10.5194/ACP-13-9899-2013, 2013.

460 Tompkins, A. M.: Organization of tropical convection in low vertical wind shears: The role of cold pools, J. Atmos. Sci., 58, 1650–1672, https://doi.org/10.1175/1520-0469(2001)058<1650:OOTCIL>2.0.CO;2, 2001.

Torri, G., Kuang, Z., and Tian, Y.: Mechanisms for convection triggering by cold pools, Geophys. Res. Lett., 42, 1943–1950, https://doi.org/10.1002/2015GL063227, 2015.

Vaisala: Weather Transmitter WXT530 Series user guide, https://www.vaisala.com/sites/default/files/documents/
465 WXT530-User-Guide-in-English-M211840EN-E.pdf, accessed on 14 January 2021, 2020.

van den Heever, S. C., Grant, L. D., Freeman, S. W., Marinescu, P. J., Barnum, J., Bukowski, J., Casas, E., Drager, A. J., Fuchs, B., Herman, G. R., Hitchcock, S. M., Kennedy, P. C., Nielsen, E. R., Park, J. M., Rasmussen, K., Razin, M. N., Riesenberg, R., Dellaripa, E. R., Slocum, C. J., Toms, B. A., and van den Heever, A.: The Colorado State University Convective CLoud Outflows and UpDrafts Experiment (C3LOUD-Ex), Bull. Am. Meteorol. Soc., 102, E1283–E1305, https://doi.org/10.1175/BAMS-D-19-0013.1, 2021.
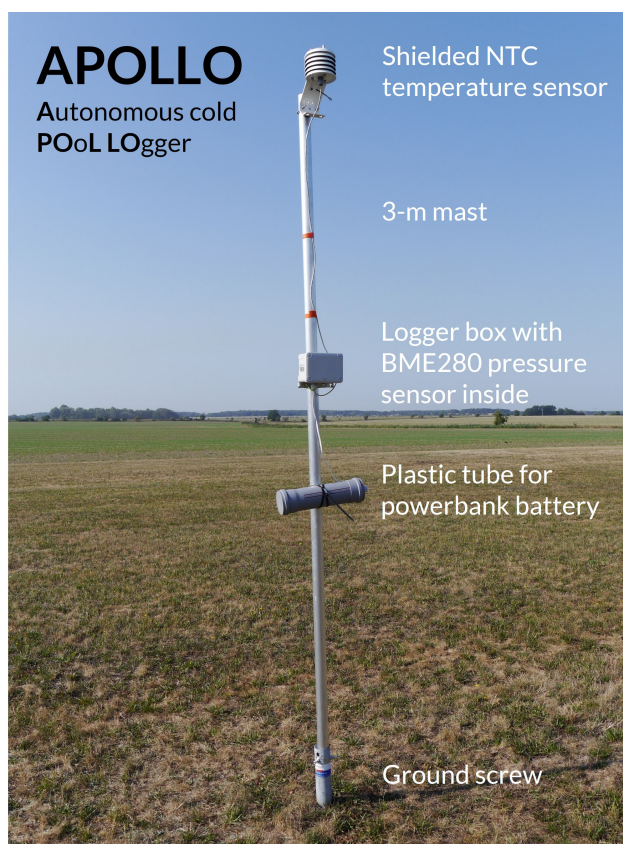
**Figure 1.** Components of APOLLO station.
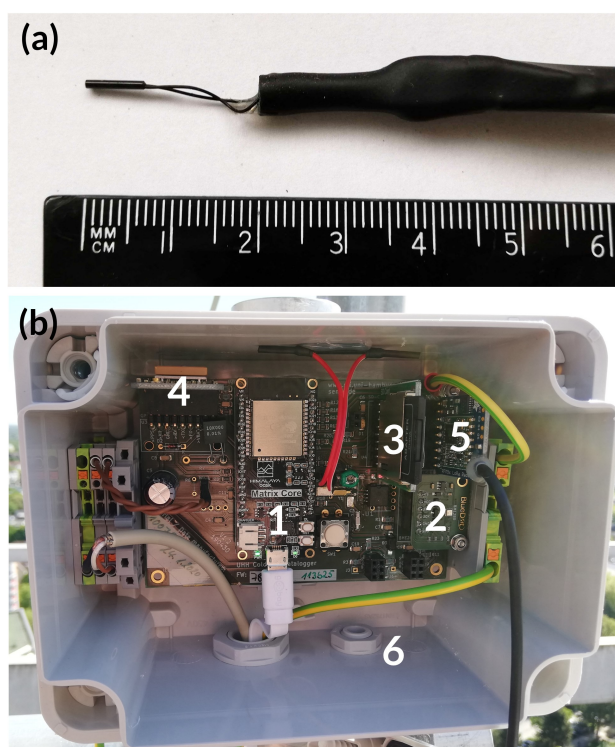
**Figure 2.** (a) NTC thermometer with scale for reference, (b) logger main board of APOLLO station. Marked are the micro controller board (1), digital air pressure sensor BME280 (2), micro-SD memory card (3), GPS receiver module (4), LoRa module (5) and pressure counterbalance valve (6).
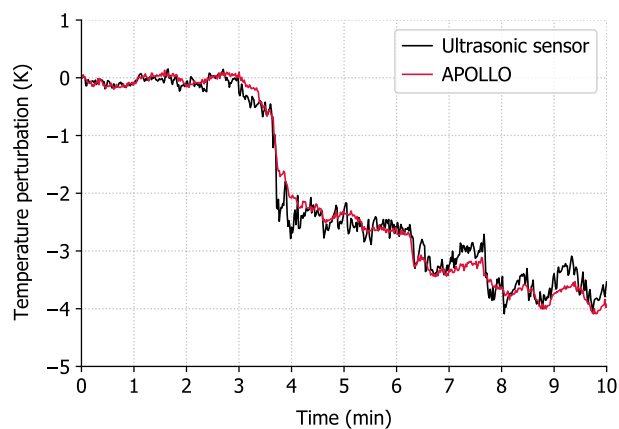
**Figure 3.** Air temperature perturbation observed by co-located ultrasonic sensor and APOLLO station during a cold pool event at the Meteorological Observatory Lindenberg (eastern Germany) on 26 August 2019. The readings of the ultrasonic sensor are 1 s averages of 20 Hz acoustic temperature measurements by an ultrasonic anemometer.
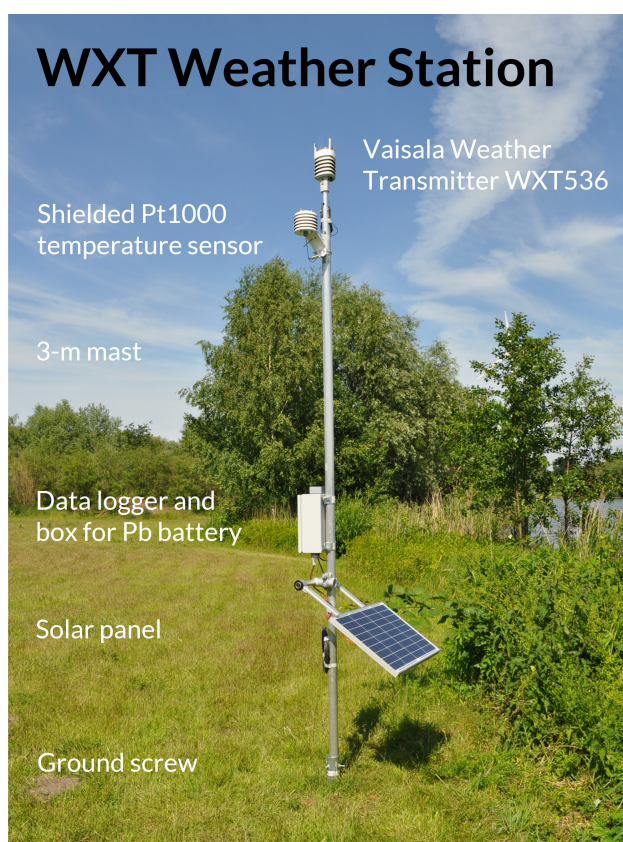
**Figure 4.** Components of WXT weather station.
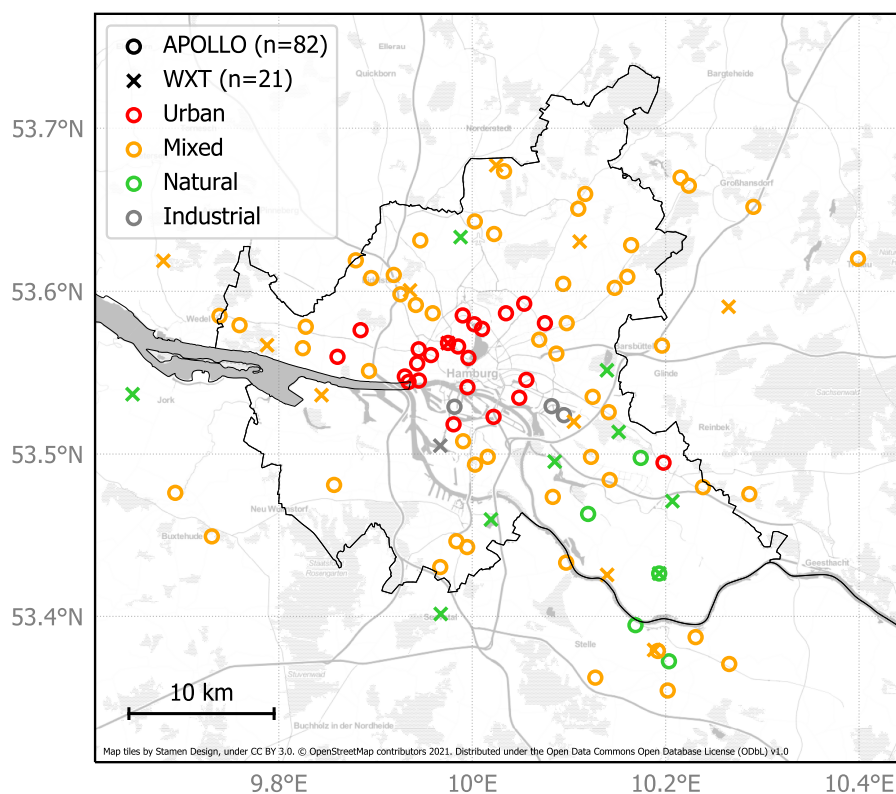
**Figure 5.** Map of APOLLO and WXT weather stations forming the FESST@HH network. Colors indicate environmental conditions of measurement sites grouped into urban (local climate Zone 2, 4 or 5), mixed (LCZ 6), natural (LCZ 9, B or D) and industrial (LCZ 8 or 10) following the framework of Stewart and Oke (2012). For stations falling into two LCZs, only the predominant sub-class is considered. Black lines mark the city limits of Hamburg.
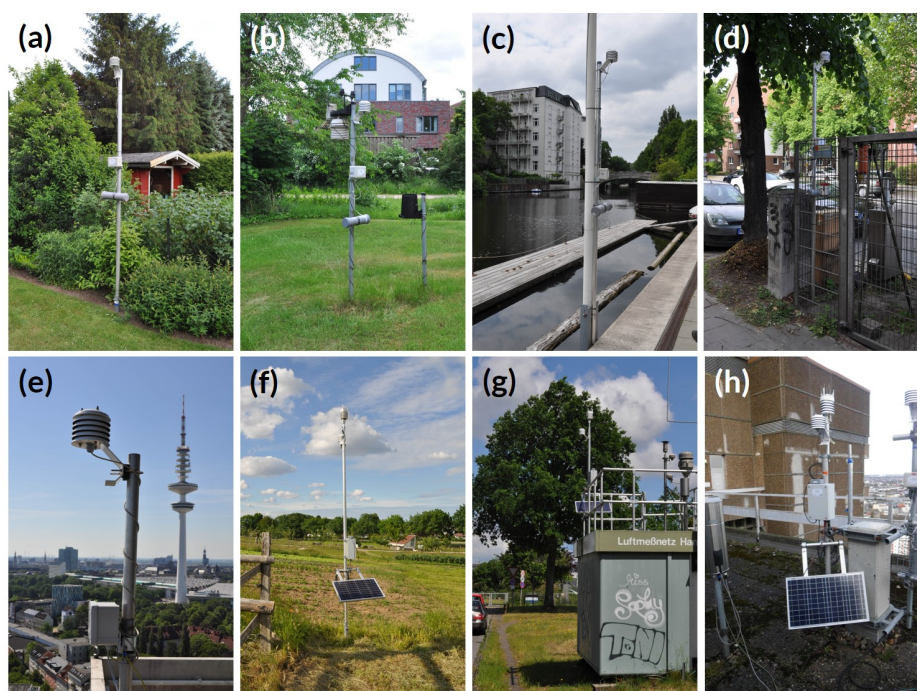
**Figure 6.** Examples of instrument installations during FESST@HH: APOLLO station (a) as the standard installation in a private garden, (b) attached to an existing weather station on a schoolyard, (c) on a boat landing stage at a channel, (d) on an air quality observation site at a public road, (e) on the balcony of the building of the Meteorological Institute, and WXT weather station (f) as the standard installation on an agricultural field, (g) on top of a container, and (h) on the roof-deck of the building of the Meteorological Institute.
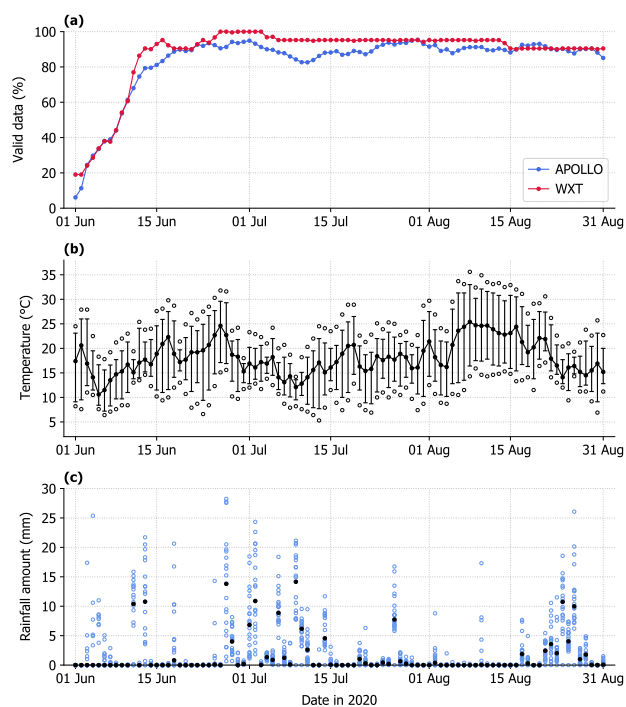
**Figure 7.** FESST@HH level 2 data from 1 June to 31 August 2020: (a) Daily mean fraction of valid temperature observations over all APOLLO and WXT stations, (b) daily median (filled dots), 5 %-quantile and 95 %-quantile (whiskers) and minimum and maximum (open circles) of all WXT air temperature observations, (c) individual accumulated rainfall amount at all WXT stations (open circles). Filled dots mark the daily median.
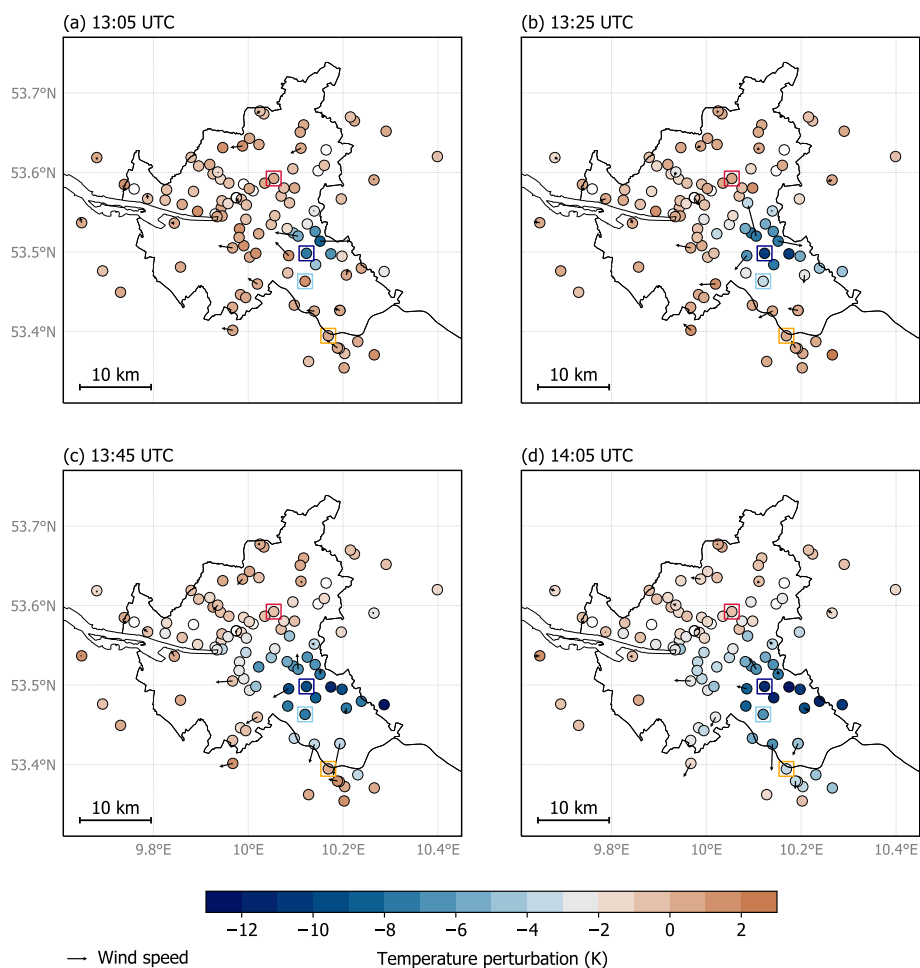
**Figure 8.** Perturbation in air temperature since 12:30 UTC from (a) 13:05 UTC to (d) 14:05 UTC observed by APOLLO and WXT stations during a cold pool event on 10 August 2020. Bluish colors mark stations inside the cold pool, defined by a temperature perturbation smaller than -2 K (color map by Crameri (2018); Crameri et al. (2020)). Black arrows indicate instantaneous wind speed and direction observed by WXT stations. Length of reference arrow refers to $5\,\mathrm{m\,s^{-1}}$ wind speed. The four highlighted stations refer to the respective data illustrated in Fig. 9.
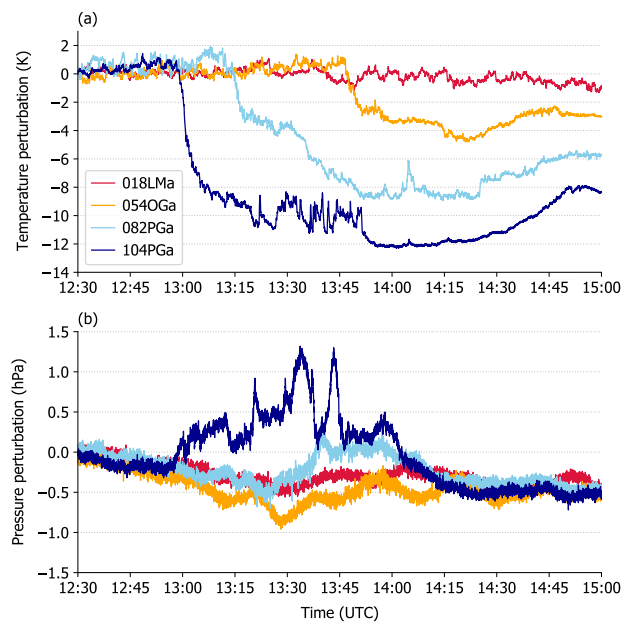
**Figure 9.** Perturbation in (a) air temperature and (b) pressure since 12:30 UTC observed by the four selected APOLLO stations *Luftmessnetz Habichtstraße* (018LMa), *Obsthof Lehmbeck* (054OGa), *Ochsenwerder Norderdeich* (082PGa) and *Luxweg* (104PGa) during a cold pool event on 10 August 2020. Locations of the stations are also highlighted in Fig. 8.
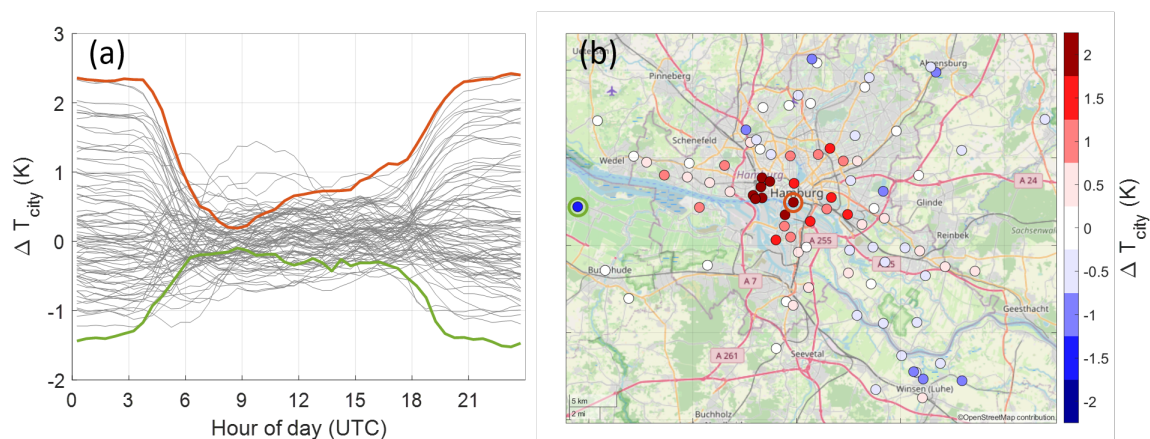
**Figure 10.** (a) Mean diurnal cycle of urban temperature modification $\Delta T_{\mathrm{city}}$ and (b) nighttime (21:00 UTC to 03:00 UTC) mean of $\Delta T_{\mathrm{city}}$ at all APOLLO and WXT stations from 15 June to 31 August 2020. Highlighted in orange and green are the stations *Wetterstation HafenCity* (010WSa) and *Obsthof Schuback* (055OGw), respectively. © OpenStreetMap contributors 2021. Distributed under the Open Data Commons Open Database License (ODbL) v1.0.
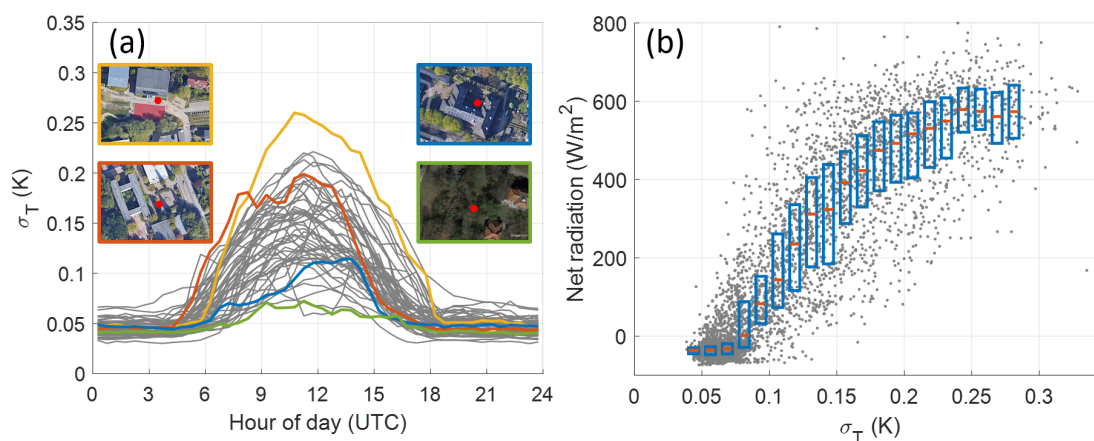
**Figure 11.** (a) Mean diurnal cycle of standard deviation of 1 min temperature fluctuations $\sigma_T$ at all APOLLO stations (grey lines) and at the highlighted stations *Stadtteilschule Blankenese* (yellow; 033KBa), *Schule Redder* (orange; 036KBa), *Luftmessnetz Rothenburgsort* (blue; 020LMa) and *Uni Sternwarte* (green; 043UHa). Map data © Google Earth 2021. (b) Net radiation at the Hamburg weather mast site dependent on $\sigma_T$ at station *Wetterstation Zollamt*, both averaged over 10 min. Blue boxes and orange bars indicate the inter-quartile range and median for the respective $\sigma_T$ bin. The analyses in both (a) and (b) are valid for sunny days from 1 June to 31 August 2020, whereas sunny days are defined as days on which the daily averaged global radiation at Hamburg weather mast is larger than at least one-third of the daily averaged theoretical maximum of clear sky insolation.

**Table 1.** Sensor specifications of APOLLO station (TE Connectivity, 2015; Bosch, 2020).

| Parameter | Sensor | Measurement range | Accuracy |
|---|---|---|---|
| Temperature | NTC thermistor | -40 ... 100 °C | ±0.2 K at 0 ... 70 °C |
| Pressure | BME280 digital sensor | 300 ... 1100 hPa | ±1 hPa at 0 ... 30 °C (absolute) |
| | | | ±0.12 hPa at 25 ... 40 °C (relative) |

**Table 2.** Sensor specifications of WXT weather station (Vaisala, 2020).

| Parameter | Sensor | Measurement range | Accuracy |
|---|---|---|---|
| Temperature | PTU module | -52 ... 60 °C | ±0.3 K at 20 °C |
| | Pt1000 thermometer | -50 ... 85 °C | ±1.3 K at 20 °C |
| Pressure | PTU module | 500 ... 1100 hPa | ±0.5 hPa at 0 ... 30 °C |
| | | | ±1.0 hPa at -52 ... 60 °C |
| Relative humidity | PTU module | 0 ... 100 %RH | ±3 %RH at 0 ... 90 %RH |
| | | | ±5 %RH at 90 ... 100 %RH |
| Wind speed | Ultrasonic anemometer | 0 ... 60 m s$^{-1}$ | ±3 % at 10 m s$^{-1}$ |
| Wind direction | Ultrasonic anemometer | 0 ... 360° | ±3° at 10 m s$^{-1}$ |
| Rainfall | Piezoelectrical sensor | - | better than 5 %, weather dependent |

**Table 3.** Meta data of APOLLO measurement sites. Altitude denotes the height of ground above sea level and sensor height is the height of temperature sensor above ground. See section 3.1 for explanation of local climate zones (LCZ) after Stewart and Oke (2012).

| Identifier | Name | Latitude (°N) | Longitude (°E) | Altitude (m) | Sensor height (m) | LCZ |
|---|---|---|---|---|---|---|
| 007WSa | Wetterstation Stellingen Wohngebiet | 53.59817 | 9.92575 | 21 | 3 | 6 |
| 008WSa | Wetterstation Wilhelmsburg Grünfläche | 53.49349 | 10.00290 | 3 | 3 | 6 |
| 010WSa | Wetterstation HafenCity | 53.54109 | 9.99505 | 8 | 2 | 5 |
| 011WSa | Wetterstation Zollamt | 53.52393 | 10.09486 | 6 | 3 | 8 |
| 015LMa | Luftmessnetz Max-Brauer-Allee | 53.55571 | 9.94306 | 25 | 3 | 2 |
| 016LMa | Luftmessnetz Kieler Straße | 53.56440 | 9.94464 | 17 | 3 | 2 |
| 018LMa | Luftmessnetz Habichtstraße | 53.59240 | 10.05374 | 13 | 3 | 5 |
| 019LMa | Luftmessnetz Elbhang | 53.54523 | 9.94488 | 23 | 3 | 5 |
| 020LMa | Luftmessnetz Rothenburgsort | 53.53463 | 10.04861 | 4 | 3 | 5 |
| 021LMa | Luftmessnetz Stresemannstraße | 53.56086 | 9.95733 | 21 | 3 | 2 |
| 022LMa | Luftmessnetz Neugraben | 53.48101 | 9.85715 | 3 | 3 | 6 |
| 023LMa | Luftmessnetz Wilhelmsburg | 53.50789 | 9.99059 | 3 | 3 | 6 |
| 024LMa | Luftmessnetz Hafen | 53.52910 | 9.98163 | 6 | 3 | 8 |
| 025LMa | Luftmessnetz Veddel | 53.52287 | 10.02204 | 5 | 3 | 5G |
| 026LMa | Luftmessnetz Billbrook | 53.52945 | 10.08207 | 5 | 3 | 8G |
| 027KBa | Saselbekstraße, Sasel | 53.65976 | 10.11679 | 30 | 3 | 6 |
| 028KBa | Halepaghen Schule, Buxtehude | 53.47613 | 9.69293 | 3 | 2 | 6 |
| 029KBa | Stadtteilschule Eidelstedt | 53.60816 | 9.89548 | 19 | 3 | 6 |
| 030KBa | Stadtteilschule Meiendorf | 53.62835 | 10.16431 | 40 | 2 | 6 |
| 031KBa | Gymnasium Rahlstedt | 53.60212 | 10.14735 | 31 | 2 | 6 |
| 033KBa | Stadtteilschule Blankenese | 53.56509 | 9.82479 | 39 | 3 | 6 |
| 036KBa | Schule Redder, Sasel | 53.65064 | 10.10965 | 38 | 2 | 6 |
| 037UHa | Uni Physik DESY, Bahrenfeld | 53.57615 | 9.88457 | 38 | 3 | 5 |
| 039UHa | Uni Campus, Rotherbaum | 53.56615 | 9.98540 | 12 | 3 | 5 |
| 040UHa | Geomatikum, Balkon 16. Stock | 53.56831 | 9.97495 | 16 | 68 | 4 |
| 041UHa | Uni Botanischer Garten, Klein Flottbek | 53.55979 | 9.86068 | 29 | 3 | 5 |
| 043UHa | Uni Sternwarte, Bergedorf | 53.47964 | 10.23859 | 31 | 3 | 6A |
| 046OGa | BAW Rissen | 53.58492 | 9.73867 | 11 | 3 | 6A |
| 049OGa | Horner Rennbahn | 53.56176 | 10.08700 | 14 | 3 | 6 |
| 051OGa | Drachenwiese Winsen | 53.37231 | 10.20341 | 4 | 3 | B |
| 052OGa | HAW Campus Bergedorf | 53.49469 | 10.19780 | 19 | 3 | 5 |
| 053OGa | Hamburger Bogengilde, Fuhlsbüttel | 53.64289 | 10.00270 | 21 | 3 | 6D |
| 054OGa | Obsthof Lehmbeck, Hoopte | 53.39460 | 10.16881 | 3 | 3 | 9 |

| Identifier | Name | Latitude (°N) | Longitude (°E) | Altitude (m) | Sensor height (m) | LCZ |
|---|---|---|---|---|---|---|
| 057OGa | Segelclub Rhe, Rotherbaum | 53.55912 | 9.99605 | 4 | 3 | 5G |
| 059OGa | Uni Segelclub, Uhlenhorst | 53.57696 | 10.01017 | 5 | 3 | 5G |
| 060OGa | Uni Rudersteg, Eppendorf | 53.58521 | 9.99019 | 4 | 3 | 5G |
| 061OGa | Bootssteg Bobby Reich, Winterhude | 53.57979 | 10.00210 | 3 | 3 | 5G |
| 063OGa | Immanuel-Kant Gymnasium, Marmstorf | 53.43041 | 9.96692 | 41 | 3 | 6 |
| 066OGa | Tennisclub Eichtalpark, Wandsbek | 53.58045 | 10.09769 | 13 | 3 | 6A |
| 068OGa[1] | Billwerder Billdeich, Oberbillwerder | 53.49763 | 10.17424 | 2 | 3 | 9 |
| 069OGa | Europaring, Winsen | 53.35427 | 10.20215 | 6 | 3 | 6 |
| 070PGa | Ilmenaudeich, Tönnhausen | 53.37063 | 10.26575 | 4 | 3 | 6 |
| 071PGa | Laßrönner Dorfstraße, Laßrönne | 53.38721 | 10.23099 | 4 | 3 | 6 |
| 072PGa | Hoopter Straße, Stöckte | 53.37869 | 10.19198 | 3 | 3 | 6 |
| 073PGa | Im Schönenfelde, Wilhelmsburg | 53.49830 | 10.01601 | 2 | 3 | 6 |
| 074PGa | Am Eisenwerk, Jarrestadt | 53.58654 | 10.03488 | 8 | 3 | 5 |
| 075PGa | Himmelshorst, Großhansdorf | 53.65183 | 10.29073 | 49 | 3 | 6 |
| 076PGa | Gartenstraße, Trittau | 53.62002 | 10.39891 | 42 | 2 | 6 |
| 077PGa | Hamburger Straße, Ahrensburg | 53.66481 | 10.22399 | 47 | 3 | 6 |
| 078PGa | Waldweg, Immenbeck | 53.44932 | 9.73072 | 22 | 2 | 6 |
| 079PGa | Sumpfveilchenweg, Langenhorn | 53.67367 | 10.03292 | 32 | 3 | 6 |
| 080PGa | Lupinenkamp, Fuhlsbüttel | 53.63517 | 10.02261 | 22 | 3 | 6 |
| 082PGa | Ochsenwerder Norderdeich, Ochsenwerder | 53.46314 | 10.11983 | 2 | 3 | 9 |
| 083PGa[2] | Norderquerweg, Kirchwerder | 53.42645 | 10.19333 | 2 | 3 | D |
| 084PGa | Overdeich, Over | 53.43314 | 10.09711 | 3 | 3 | 6 |
| 085PGa | Jahnstraße, Ashausen | 53.36222 | 10.12728 | 21 | 3 | 6 |
| 086PGa | Kleingartenverein Wilstorf | 53.44632 | 9.98363 | 28 | 3 | 6 |
| 087PGa | Brookwisch, Iserbrook | 53.57825 | 9.82787 | 26 | 3 | 6 |
| 088PGa | Achter de Höf, Rissen | 53.57922 | 9.75940 | 23 | 3 | 6 |
| 089PGa | Kleingartenverein Stellingen | 53.59163 | 9.94172 | 18 | 3 | 6 |
| 090PGa | Kleingartenverein Lokstedt | 53.58656 | 9.95912 | 14 | 3 | 6 |
| 091PGa | Fährstraße, Wilhelmsburg | 53.51829 | 9.98068 | 4 | 3 | 5 |
| 092PGa | Holländische Reihe, Ottensen | 53.54770 | 9.93032 | 31 | 15 | 2 |

[1] APOLLO station replaced on 25 June 2020

[2] APOLLO station replaced by WXT station on 25 June 2020

| Identifier | Name | Latitude (°N) | Longitude (°E) | Altitude (m) | Sensor height (m) | LCZ |
|---|---|---|---|---|---|---|
| 093PGa | Kleingartenverein Niendorfer Gehege | 53.61008 | 9.91888 | 12 | 3 | 6 |
| 094PGa | Harzburger Weg, Niendorf | 53.63124 | 9.94628 | 21 | 3 | 6 |
| 095PGa | Rantzaustraße, Ahrensburg | 53.66977 | 10.21542 | 47 | 3 | 6 |
| 096PGa | Godenwind, Mümmelmannsberg | 53.52577 | 10.14109 | 30 | 3 | 6 |
| 097PGa | Parchimer Straße, Rahlstedt | 53.60891 | 10.16041 | 30 | 3 | 6 |
| 098PGa | Musilweg, Wilstorf | 53.44273 | 9.99474 | 27 | 3 | 6 |
| 099PGa | Schlossgarten, Wandsbek | 53.57030 | 10.06929 | 13 | 3 | 6 |
| 100PGa | Hamfelderedder, Börnsen | 53.47537 | 10.28655 | 55 | 3 | 6 |
| 102PGa | Abelke-Bleken-Ring, Ochsenwerder | 53.47363 | 10.08330 | 1 | 3 | 6 |
| 103PGa | Burbekstraße, Eidelstedt | 53.61903 | 9.87959 | 22 | 3 | 6 |
| 104PGa | Luxweg, Billwerder | 53.49826 | 10.12280 | 1 | 3 | 6 |
| 105PGa | Barsbütteler Landstraße, Barsbüttel | 53.56667 | 10.19619 | 37 | 3 | 6 |
| 106PGa | Kleingartenverein Allermöhe | 53.48406 | 10.14210 | 2 | 3 | 6 |
| 107PGa | Ansorgestraße, Othmarschen | 53.55108 | 9.89326 | 23 | 3 | 6 |
| 108PGa | Auf dem Königslande, Wandsbek | 53.58045 | 10.07517 | 15 | 3 | 5 |
| 109PGa | Eenstock, Bramfeld | 53.60457 | 10.09405 | 18 | 3 | 6 |
| 111OGa | Suntrace, Altona | 53.54436 | 9.93413 | 5 | 10 | 5G |
| 112PGa | Teubnerweg, Billstedt | 53.53520 | 10.12454 | 17 | 3 | 6 |
| 113PGa | Steinbeker Straße, Hamm | 53.54563 | 10.05597 | 6 | 7 | 5G |

**Table 4.** As Table 3, but for WXT measurement sites.

| Identifier | Name | Latitude (°N) | Longitude (°E) | Altitude (m) | Sensor height (m) | LCZ |
|---|---|---|---|---|---|---|
| 002MIw | Wettermast, Billwerder | 53.51996 | 10.10515 | 1 | 3 | 6D |
| 004MIw | Wasserwerk Baursberg, Blankenese | 53.56692 | 9.78784 | 82 | 2 | 6 |
| 005WSw | Wetterstation Langenhorn Grünfläche | 53.67731 | 10.02480 | 24 | 3 | 6B |
| 006WSw | Wetterstation Stellingen Grünfläche | 53.60056 | 9.93568 | 14 | 3 | 6B |
| 017LMw | Luftmessnetz Finkenwerder | 53.53621 | 9.84419 | 6 | 5 | 6 |
| 035KBw | Gut Karlshöhe, Bramfeld | 53.63052 | 10.11114 | 31 | 3 | 6 |
| 044OGw | Fährhaus Tatenberg | 53.49537 | 10.08528 | 2 | 3 | 9 |
| 045OGw | Windpark Curslack | 53.47102 | 10.20700 | 2 | 3 | D |
| 047OGw | Bogenwiese Holm | 53.61872 | 9.68062 | 15 | 3 | 6 |
| 048OGw[1] | Segelflugplatz Boberg | 53.51360 | 10.15142 | 2 | 3 | 9 |
| 050OGw | Bogenschießplatz Stöckte | 53.37930 | 10.18809 | 1 | 3 | 6D |
| 055OGw | Obsthof Schuback, Mittelnkirchen | 53.53679 | 9.64878 | 1 | 3 | B |
| 062OGw | Segelverein Neuländer See | 53.45972 | 10.01936 | 1 | 3 | 9G |
| 064OGw | Biohof Obermeyer, Emmelndorf | 53.40151 | 9.96742 | 49 | 3 | 9 |
| 065OGw | Greenpeace, Wilhelmsburg | 53.50515 | 9.96698 | 8 | 3 | 10G |
| 067OGw | DWD Flughafen, Fuhlsbüttel | 53.63327 | 9.98796 | 9 | 3 | 9 |
| 081PGw | Süderquerweg, Kirchwerder | 53.42561 | 10.13946 | 3 | 3 | 6 |
| 083PGw | Norderquerweg, Kirchwerder | 53.42645 | 10.19333 | 2 | 3 | D |
| 101PGw | Reinbeker Weg, Brunsbek | 53.59054 | 10.26513 | 58 | 3 | 6 |
| 110OGw | Öjendorfer See, Billstedt | 53.55152 | 10.13930 | 13 | 3 | B |
| 114UHw[2] | Geomatikum, Dachterasse 18. Stock | 53.56819 | 9.97483 | 16 | 72 | 4 |

[1] WXT536 sensor replaced on 31 July 2020

[2] WXT536 sensor replaced on 10 June 2020